Crystal Structures and Magnetic Properties of the Manganese Oxide Chlorides Sr_2MnO_3Cl and $Sr_4Mn_3O_{8-y}Cl_2$

Christopher S. Knee,[†] Alexander A. Zhukov,[‡] and Mark T. Weller*,[†]

Departments of Chemistry and Physics and Astronomy, University of Southampton, Southampton, SO17 1BJ United Kingdom

Received March 19, 2002. Revised Manuscript Received July 31, 2002

The crystal structures of the manganese oxide chlorides Sr_2MnO_3Cl and $Sr_4Mn_3O_{8-y}Cl_2$ have been determined from neutron powder diffraction data collected at room temperature and at 2 K. The materials crystallize in the tetragonal space groups $P4/nmm$ (Sr_2MnO_3Cl) and $I4/mmm$ ($Sr_4Mn_3O_{8-y}Cl_2$) and the structures are analogous to the $n = 1$ and $n = 3$ Ruddlesden−Popper phases Sr_2MnO_4 and $Ca_4Mn_3O_{10}$. Both materials contain layers of highly distorted $Mn(III)O_5Cl$ octahedra. $Sr_4Mn_3O_{8-y}Cl_2$, in addition, has a central layer of $MnO_{6-\delta}$ octahedra with oxygen vacancies localized within the tetragonal plane. Consequently, the average coordination of the site is reduced to a mixture of 6-fold and 5-fold and some of the Mn atoms adopt pyramidal coordination. The level of oxygen deficiency within $Sr_4Mn_3O_{8-y}Cl_2$ $y = 0.44$ confirms the Mn valence is predominantly +3. Magnetic susceptibility measurements indicate the onset of antiferromagnetic ordering (T_{AF}) in the materials at 80 and 90 K for Sr_2MnO_3Cl and $Sr_4Mn_3O_{8-y}Cl_2$, respectively. Antiferromagnetic order is confirmed by the presence of magnetic scattering in the low-temperature neutron diffraction data. The magnetic structure of Sr_2MnO_3Cl has been determined, yielding an ordered manganese moment $\mu_z = 3.74(5)\ \mu_B$ at 2 K. In contrast, the magnetic scattering exhibited by $Sr_4Mn_3O_{8-y}Cl_2$ suggests a level of magnetic frustration.

Introduction

The search for new layered transition metal oxides which exhibit unusual cooperative phenomena has also led to the development of novel mixed anion systems, such as oxide carbonates,[1] oxide nitrides,[2] and oxide halides.[3] Generally, these systems offer enhanced flexibility over pure oxides both from a structural viewpoint and their ability to control the transition metal oxidation state. A specific example of this is provided by the superconducting oxyfluoride $Sr_2CuO_2F_{2+\delta}$[4] that belongs to a large family of copper oxide halide superconductors developed from the K_2NiF_4 oxychloride $Sr_2CuO_2Cl_2$.[5] Oxyhalide chemistry has been extended to other first-row transition metals with phases such as the iron materials, Ca_2FeO_3Cl and $Sr_3Fe_2O_5Br_2$ reported by Ackerman,[6] and the strontium cobalt oxychlorides, Sr_2CoO_3Cl, $Sr_2Co_2O_5Cl_2$ and $Sr_4Co_3O_{7.5}Cl_2$ reported by Cava and co-workers.[7,8] These materials all adopt Ruddlesden−Popper (RP) related structures in which either one, for example, Sr_2CoO_3Cl, or both, for example, $Sr_2Co_2O_5Cl_2$, of the terminal apical oxygen positions of the repeat perovskite block have been replaced by a halide.

Recently, we expanded this family of oxyhalides with the synthesis of the cobalt(II) phases $Sr_2CoO_2X_2$ (X = Cl and Br),[9] and the report, as a communication, of the first manganese oxychlorides Sr_2MnO_3Cl and $Sr_4Mn_3O_{8-y}Cl_2$.[10] Manganates adopting RP structures have of course been the focus of considerable interest due to the magnetoresistance properties they exhibit.[11,12] In this paper we present the results of a neutron powder diffraction study on Sr_2MnO_3Cl and $Sr_4Mn_3O_{8-y}Cl_2$ aimed at furthering our understanding of their crystal structures and, therefore, their suitability as magnetoresistive phases. The magnetic behavior of the materials has also been investigated using susceptibility measurements, and these data, combined with low-temperature neutron diffraction data, has allowed the magnetic structure of Sr_2MnO_3Cl to be determined.

* To whom correspondence should be addressed. Tel./Fax: 00 44 2380 593592. E-mail: mtw@soton.ac.uk.
[†] Department of Chemistry.
[‡] Department of Physics and Astronomy.

(1) Yamaura, K.; Huang, Q.; Lynn, J. W.; Erwin, R. W.; Cava, R. J. *J. Solid State Chem*. **2000**, *152*, 374.
(2) Veith, G. M.; Greenblatt, M.; Croft, M.; Goodenough, J. B. *Mater. Res. Bull.* **2001**, *36*, 1521.
(3) Huang, R. D.; Hoffmann, R. D.; Sleight, A. W. *Mater. Res. Bull.* **1990**, *25*, 1085.
(4) Almamouri, M.; Edwards, P. P.; Greaves, C.; Slaski, M. *Nature* **1994**, *369*, 382.
(5) Grande, B.; Müller-Buschbaum, Hk. *Z. Anorg. Allg. Chem*. **1975**, *417*, 68.
(6) Ackerman, J. F. *J. Solid State Chem*., **1991**, *92*, 496.
(7) Mcglothlin, N.; Ho, D. Cava, R. J. *Mater. Res. Bull.* **2000**, *35*, 1035.
(8) Loureiro, S. M.; Felser, C.; Huang, Q.; Cava, R. J. *Chem. Mater.* **2000**, *12*, 3181.
(9) Knee, C. S.; Weller, M. T. *J. Solid State Chem*. **2002**, *168*, 1.
(10) Knee, C. S.; Weller, M. T. *Chem. Commun*. **2002**, 256.
(11) Morimoto, Y.; Asamitsu, A.; Kuwahara, H.; Tokura, Y. *Nature* **1996**, *380*, 141.
(12) Battle, P. D.; Green, M. A.; Laskey, N. S.; Millburn, J. E.; Radaelli, P. G.; Rosseinsky, M. J.; Sullivan, S. P.; Vente, J. F. *Phys. Rev. B* **1996**, *54*, 15967.

10.1021/cm020280c CCC: $22.00
Published on Web 09/21/2002

Experimental Section

Polycrystalline samples of Sr_2MnO_3Cl (2 g) and $Sr_4Mn_3O_{8-y}Cl_2$ (1.5 g) were synthesized by reacting high-purity reagents, SrO, $SrCl_2$, and Mn_2O_3, in evacuated silica ampules using the method described in ref 10. Phase purity was assessed from powder X-ray data collected using a Bruker D8 diffractometer (Cu $K\alpha_1$) operating with a position-sensitive detector. The only impurity apparent for $Sr_4Mn_3O_{8-y}Cl_2$ was a trace level of MnO while the Sr_2MnO_3Cl sample contained a small level (≈10%) of the three-layer phase. Time-of-flight neutron powder diffraction data were collected on $Sr_4Mn_3O_{8-y}Cl_2$ at room temperature and 2 K and on Sr_2MnO_3Cl at 2 K using the medium-resolution diffractometer POLARIS located at the Rutherford Appleton Laboratory, U.K. A room-temperature scan for Sr_2MnO_3Cl was also collected using the GEM instrument at the same facility. For the subsequent structural refinements data from the higher resolution C-bank of POLARIS (0.2−3.2 Å) were analyzed, while a multihistogram approach combining four detector banks was used for the GEM data. Magnetic reflections were detected at d spacings >3.5 Å in the lower resolution A-bank of POLARIS (0.5−8.3 Å) for both phases. The diffraction data were analyzed using the GSAS software package[13] with the structural models previously reported from powder X-ray data analyses[10] employed in initial cycles. The magnetic susceptibility of the materials in the temperature range 290−10 K were determined using a Cryogenics S600 SQUID magnetometer. Data were collected after cooling the sample in the absence of an applied field (ZFC) and after cooling in the measuring field (FC) of 1 T.

Results

Crystal Structure Refinement. Refinement of the structural coordinates and isotropic atomic displacement parameters for Sr_2MnO_3Cl at room temperature proceeded smoothly to convergence. Variation of the site occupancies produced no significant deviations from the X-ray model. The only anomaly was a slightly large atomic displacement parameter (ADP) for the chloride ion which was resolved by the introduction and refinement of an anisotropic ADP for the site producing an appreciable improvement in the fit. The 2 K refinement followed a similar route with the exception that the thermal parameters for the Sr(1) and Mn sites now took small (nonphysical) negative values. This was attributed to absorption effects and corrected through the introduction of an absorption coefficient for the refinement. $Sr_4Mn_3O_{8-y}Cl_2$ was introduced as a secondary phase in both room temperature and 2 K analyses and refined to give a crystal phase fraction = 0.095(1). The refined structural parameters are summarized in Table 1 and the Rietveld profile fit obtained to the $2\theta = 91.3°$ bank of GEM shown in Figure 1.

For $Sr_4Mn_3O_{8-y}Cl_2$ the introduction of atomic displacement parameters into the analysis led to larger than expected values for the O(3) basal oxygen of the $Mn(2)O_6$ octahedron, for example, $U_{iso} = 3.2$ Å^2 at 2 K. Such a value indicated possible disorder and/or partial occupancy of the site. Refinement of an anisotropic ADP yielded values of $U_{11} = 0.067(2)$ Å^2, $U_{22} = 0.008(1)$ Å^2, and $U_{33} = 0.031(2)$ Å^2, strongly indicating positional disorder along the x-direction. The ion was displaced on to a half-occupied (x, $^1/_2$, 0) site, and the positional and isotopic AD parameters were refined. This resulted in an enhanced fit to the profile and reduction in the ADP, although the value obtained was still significantly higher than those of the other oxygen positions. The site occupancy was therefore varied and dropped in a stable and reproducible manner to values of 0.41(1) and 0.39(1) in the 2 K and room-temperature analyses, respectively. An anisotropic ADP was also refined for the Cl in both data sets. Finally, the small contribution to the diffraction patterns from MnO was fitted to give a refined phase fraction of 0.02(1). Once more some of the temperature factors determined from the 2 K data were smaller than physically reasonable but were corrected by the inclusion of a small absorption coefficient into the refinement. The Rietveld fit obtained for the room-temperature data is shown in Figure 2 and the derived structural parameters are displayed in Table 2. In both patterns collected at 2 K additional reflections in the positions expect for the cryostat were detected and where possible these regions were excluded from the data.

Table 1. Structural Parameters for Sr_2MnO_3Cl at Room Temperature (Top Line) and 2 K (Bottom Line), Space Group *P4/nmm*[a]

atom	site	x	y	z	$U_{iso} \times 100$ (Å^2)	n
Sr(1)	2c	$^1/_4$	$^1/_4$	0.0913(1)	0.54(4)	1.0
				0.0909(2)	0.06(4)	
Sr(2)	2c	$^1/_4$	$^1/_4$	0.3440(1)	0.86(3)	1.0
				0.3444(2)	0.24(4)	
Mn(1)	2c	$^1/_4$	$^3/_4$	0.2126(2)	0.41(5)	1.0
				0.2130(3)	0.18(6)	
O(1)	4f	$^3/_4$	$^1/_4$	0.23110(8)	0.91(3)	1.0
				0.2325(1)	0.51(4)	
O(2)	2c	$^3/_4$	$^3/_4$	0.0759(1)	0.90(4)	1.0
				0.0753(2)	0.47(5)	
Cl	2c	$^3/_4$	$^3/_4$	0.42521(1)	1.97[b]	1.0
				0.42761(2)	0.92[c]	
	a (Å)				3.84481(9)	
					3.82543(5)	
	c (Å)				14.7709(4)	
					14.7138(4)	
	μ (μ_B)				3.74(5)[d]	

[a] GEM (RT)—powder totals for four histograms: $R_{wp} = 1.96\%$, $R_p = 1.79\%$, $\chi^2 = 7.01$. POLARIS C-bank (2 K): $R_{wp} = 0.74\%$, $R_p = 1.30\%$, $\chi^2 = 2.54$. POLARIS A-bank (2 K): $R_{wp} = 1.90\%$, $R_p = 2.25\%$, $R_{Mag} = 20.9\%$, $\chi^2 = 1.45$. [b] $U_{11} = U_{22} = 0.0139(4)$, $U_{33} = 0.0312(10)$ Å^2. [c] $U_{11} = U_{22} = 0.0108(6)$, $U_{33} = 0.006(8)$ Å^2. [d] Magnetic unit cell: $a_m = b_m = \sqrt{2}a_n$ and $c_m = c_n$; $|\mu| = \mu_z$, $\mu_x = \mu_y = 0$.

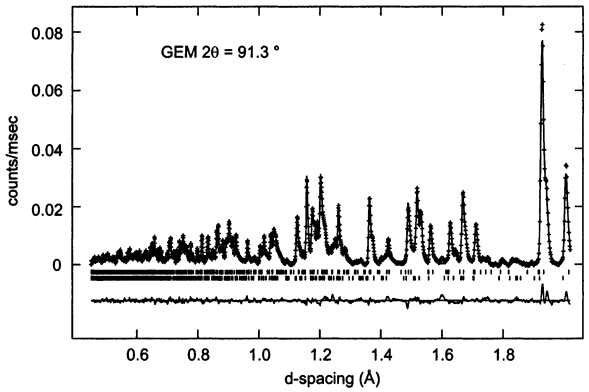

Figure 1. Rietveld fit obtained to the room-temperature neutron diffraction data collected on the $2\theta = 91.3°$ detector bank of GEM for Sr_2MnO_3Cl. Crosses are observed data, upper continuous line the fitted profile, and lower line the difference. Tick marks show the allowed reflection positions for Sr_2MnO_3Cl (lower) and $Sr_4Mn_3O_{8-y}Cl_2$ (upper).

(13) Larson, A. C.; Von Dreele, R. B. *General Structure Analysis System*; Los Alamos National Laboratory, Los Alamos, NM, 1994.

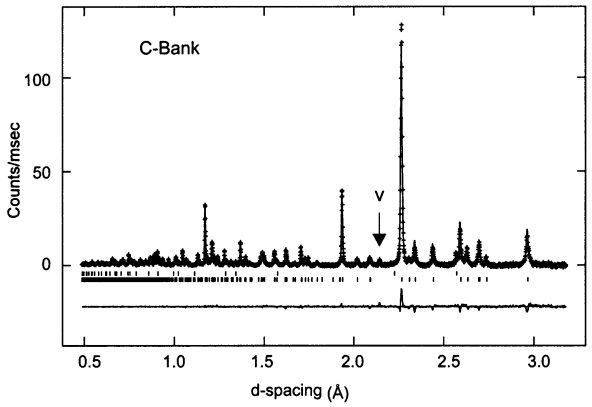

Figure 2. Rietveld fit obtained to the room-temperature neutron diffraction data collected on the C-bank of POLARIS for $Sr_4Mn_3O_{8-y}Cl_2$. Crosses are observed data, upper continuous line the fitted profile, and lower line the difference. Tick marks show the allowed reflection positions for $Sr_4Mn_3O_{8-y}Cl_2$ (lower) and MnO (upper). An additional peak due to the vanadium sample can is also indicated (V).

Table 2. Structural Parameters for $Sr_4Mn_3O_{8-y}Cl_2$ at Room Temperature (Top Line) and 2 K (Bottom Line). Space Group *I4/mmm*[a]

atom	site	*x*	*y*	*z*	$U_{iso} \times 100$ (Å^2)	*n*
Sr(1)	4e	0	0	0.43899(6)	1.11(3)	1.0
				0.43924(10)	0.61(4)	
Sr(2)	4e	0	0	0.32088(5)	0.76(3)	1.0
				0.32036(8)	0.31(3)	
Mn(1)	4e	0	0	0.12079(9)	0.52(3)	1.0
				0.1212(2)	0.24(4)	
Mn(2)	2a	0	0	0	0.48(5)	1.0
					0.26(8)	
O(1)	8g	0	1/2	0.12838(3)	0.79(2)	1.0
				0.12867(6)	0.37(3)	
O(2)	4e	0	0	0.05898(8)	1.85(4)	1.0
				0.0586(1)	1.67(9)	
O(3)	8j	0.0535(8)	1/2	0	1.12(9)	0.39(1)
		0.049(2)			0.8(1)	0.41(1)
Cl	4e	0	0	0.21572(5)	1.62[b]	1.0
				0.21563(8)	0.83[c]	
		a (Å)			3.86585(3)	
					3.85706(3)	
		c (Å)			32.2585(2)	
					32.189(1)	

[a] POLARIS C-bank (RT): $R_{wp} = 1.80\%$, $R_p = 3.82\%$, $\chi^2 = 2.54$. POLARIS C-bank (2 K): $R_{wp} = 0.66\%$, $R_p = 1.25\%$, $\chi^2 = 3.36$. [b] $U_{11} = U_{22} = 0.0114(3)$, $U_{33} = 0.0256(7)$ Å^2. [c] $U_{11} = U_{22} = 0.0026(4)$, $U_{33} = 0.0197(9)$ Å^2.

Magnetic Susceptibility. Figures 3 and 4 show the bulk magnetic susceptibility curves obtained for the compounds over the temperature range 290−10 K. The behavior of the materials is qualitatively similar, with an overall increase in susceptibility with decreasing temperature and distinct maxima, that is, $T_{(\chi max)}$, in χ at 95 and 90 K for Sr_2MnO_3Cl and $Sr_4Mn_3O_{8-y}Cl_2$, respectively. The local maxima in the susceptibility indicate the onset of antiferromagnetic (AF) correlations within both materials. However, in layered systems, particularly two-dimensional K_2NiF_4-type phases, a degree of caution is required as $T_{(\chi max)}$ does not necessarily correspond to the critical temperature of the compound. To obtain a more accurate estimate, the function $d(\chi T)/dT$ vs T was plotted.[14] This approach revealed a λ-type maximum coincident with $T_{(\chi max)}$ for

(14) Fisher, M. E. *Philos. Mag.* **1962**, *7*, 1731.

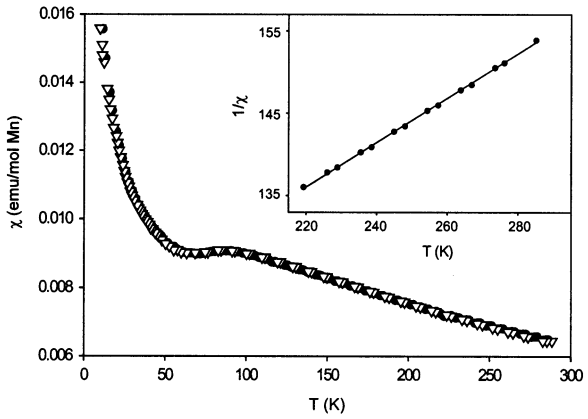

Figure 3. Magnetic susceptibility data vs temperature for Sr_2MnO_3Cl collected at 1 T. Open triangles and closed circles are ZFC and FC data, respectively. The inset shows the fit to the inverse susceptibility in the range 290−220 K.

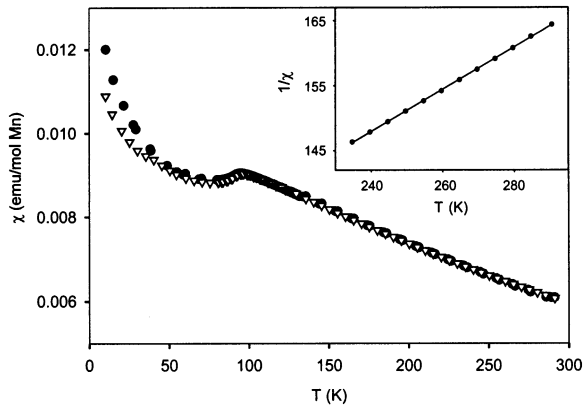

Figure 4. Magnetic susceptibility data vs temperature for $Sr_4Mn_3O_{8-y}Cl_2$ collected at 1 T. Open triangles and closed circles are ZFC and FC data, respectively. The inset shows the fit to the inverse susceptibility in the range 290−230 K.

$Sr_4Mn_3O_{8-y}Cl_2$ and a broader peak centered at 80 K for Sr_2MnO_3Cl and these values are listed as the antiferromagnetic transition temperatures (T_{AF}) in Table 4. Above the transitions Curie−Weiss-like behavior is observed (see insets of Figures 3 and 4) and Table 4 also summarizes the information extracted from this region.

Magnetic Scattering. Examination of the two low-temperature data sets collected on the large *d*-spacing A-bank of POLARIS revealed evidence of long-range AF order with the appearance of additional peaks not apparent in the room-temperature patterns for both materials (Figures 5 and 6). The observed magnetic scattering is rather different, with well-resolved peaks at 4.3, 5.1, and 5.4 Å for Sr_2MnO_3Cl and less distinct intensity in the region 5.0−5.4 Å for $Sr_4Mn_3O_{8-y}Cl_2$. The magnetic peaks detected for the single-layer phase could be indexed as the {100}, {101}, and {102} reflections of a $\sqrt{2}a_n \times \sqrt{2}b_n \times c$ magnetic cell related to the nuclear structure by the transformation vector $\mathbf{k} = (1/2, 1/2, 0)$. This behavior is consistent with AF coupling of neighboring Mn spins along all three crystallographic axes. Refinement began with the use of the structural parameters obtained from the higher resolution C-bank analysis, which were fixed to give a good fit to the nuclear peaks present in the A-bank data. The magnetic model was then introduced, with the Mn moments aligned parallel to the *c*-axis, and the magnetic intensity

Table 3. Selected Bond Distances (Å) and Angles (deg) for Sr_2MnO_3Cl and $Sr_4Mn_3O_{8-y}Cl_2$ at Room Temperature (Top Line) and 2 K (Bottom Line)

Sr_2MnO_3Cl		$Sr_4Mn_3O_{8-y}Cl_2$	
Mn(1)−O(1) ×4	1.9417(5)	Mn(1)−O(1) ×4	1.9484(4)
	1.9341(7)		1.9434(7)
Mn(1)−O(2) ×1	2.019(4)	Mn(1)−O(2) ×1	1.994(4)
	2.026(5)		2.015(6)
Mn(1)−Cl ×1	3.141(3)	Mn(1)−Cl ×1	3.062(4)
	3.157(5)		3.039(6)
O(1)−Mn(1)−O(1)	163.2(2)	O(1)−Mn(1)−O(1)	165.6(2)
	162.9(3)		165.8(3)
Sr(1)−O(1) ×4	2.821(1)	Sr(1)−O(1) ×4	2.908(2)
	2.828(2)		2.908(2)
Sr(1)−O(2) ×4	2.7282(2)	Sr(1)−O(2) ×4	2.73436(9)
	2.7147(3)		2.7282(2)
Sr(1)−O(2) ×1	2.470(3)	Sr(1)−O(3) ×4	2.907(3)−2.618(3)
	2.446(4)		2.883(5)−2.617(5)
Sr(2)−O(1) ×4	2.545(2)	Sr(2)−O(1) ×4	2.533(1)
	2.524(2)		2.532(2)
Sr(2)−Cl ×4	2.9715(9)	Sr(2)−Cl ×4	2.9777(9)
	2.969(1)		2.963(1)
Sr(2)−Cl ×1	3.409(3)	Sr(2)−Cl ×1	3.392(2)
	3.354(3)		3.371(3)
		Mn(2)−O(3) ×4	1.9439(4)
			1.9378(6)
		Mn(2)−O(2) ×2	1.903(3)
			1.887(4)
		O(3)−Mn(2)−O(3)	180
			180

Table 4. Susceptibility Maxima ($T_{(\chi max)}$), Antiferromagnetic Transition Temperatures (T_{AF}), Weiss Constants (θ), and Calculated Mn Moments for Sr_2MnO_3Cl and $Sr_4Mn_3O_{8-y}Cl_2$

	$T_{(\chi max)}$ (K)	T_{AF} (K)	θ (K)	μ_{eff} (μ_B)	μ_Z (μ_B)
Sr_2MnO_3Cl	95(4)	80(3)	−284(5)	5.4(1)	3.74(5)
$Sr_4Mn_3O_{8-y}Cl_2$	90(2)	90(1)	−215(4)	5.0(1)	−

modeled as a second phase giving a refined $\mu_z = 3.74(5)$ μ_B. Figure 5 shows the fit to the profile achieved for the 2 K A-bank data contrasted with the fit to the room-temperature data obtained from the $2\theta = 18°$ bank of GEM.

The additional weak magnetic intensity at 5.4 and 5.2 Å in the low-temperature pattern obtained for $Sr_4Mn_3O_{8-y}Cl_2$ could be tentatively indexed as the {101} and {102} reflections of a $\sqrt{2}a_n \times \sqrt{2}b_n \times c$ magnetic cell. Various attempts were made to fit these features using a number of descriptions, with both antiferromagnetic and ferromagnetic coupling within and between the Mn triple blocks considered. However, with only a few weak magnetic reflections, poorly resolved from the background, construction of a robust magnetic structure model could not be achieved. The peak at 5.1 Å could not be accounted for by a variety of supercells based on the nuclear structure of $Sr_4Mn_3O_{8-y}Cl_2$. It lies in the expected position for the strongest magnetic reflection of the impurity MnO ($T_N = 118$ K), an assignment further supported by its intensity relative to the most intense {−222} nuclear reflection.[15]

Discussion

The syntheses of the manganese oxychloride phases are readily achieved in a sealed evacuated system. This method is required to prevent oxidation of manganese and thus the formation of the Mn^{4+} phases such as $Sr_7Mn_4O_{15}$[16] that are obtained on reaction in air. The use of a reaction vessel sealed under vacuum also reduces the potential hydrolysis of the metal halide and mitigates against the loss of the more volatile metal halides at high temperature. Attempts to improve the synthesis

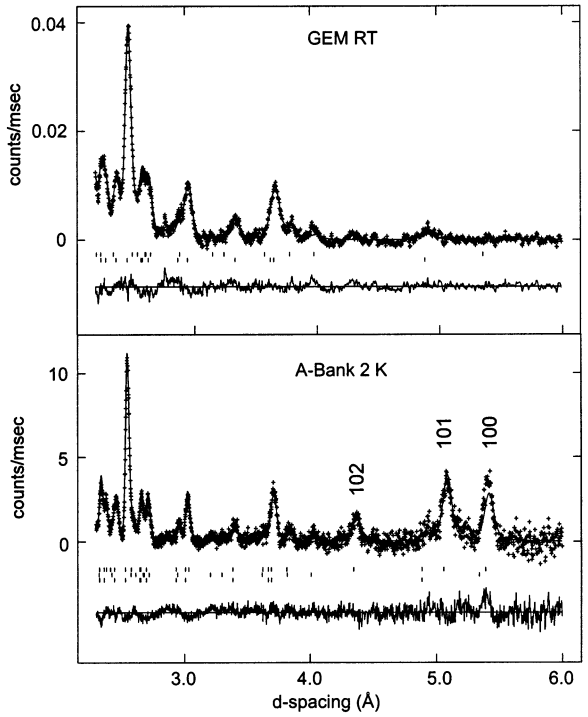

Figure 5. Rietveld fits obtained to the neutron diffraction data collected at room temperature on the $2\theta = 18°$ detector bank of GEM (top) and at 2 K on the A-bank of POLARIS for Sr_2MnO_3Cl (bottom). For the GEM data tick marks show the reflection positions for Sr_2MnO_3Cl (lower) and $Sr_4Mn_3O_{8-y}Cl_2$ (upper) while the POLARIS refinement includes nuclear Sr_2MnO_3Cl (lower), $Sr_4Mn_3O_{8-y}Cl_2$ (middle), and magnetic Sr_2MnO_3Cl (upper) phases.

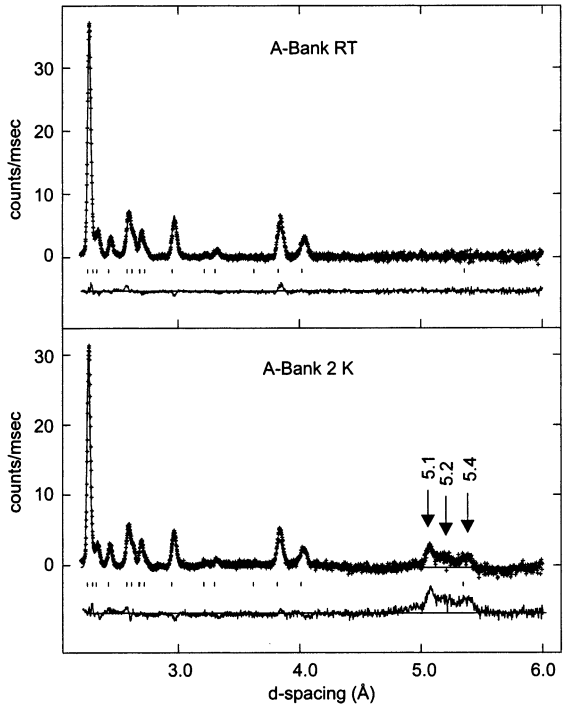

Figure 6. Rietveld fits obtained to the neutron diffraction data collected at room temperature (top) and at 2 K (bottom) on the A-bank of POLARIS for $Sr_4Mn_3O_{8-y}Cl_2$. The tick marks denote allowed reflection positions for $Sr_4Mn_3O_{8-y}Cl_2$.

(15) Shaked, H.; Faber, J., Jr.; Hitterman, R. L. *Phys. Rev. B* **1988**, *38*, 11901.

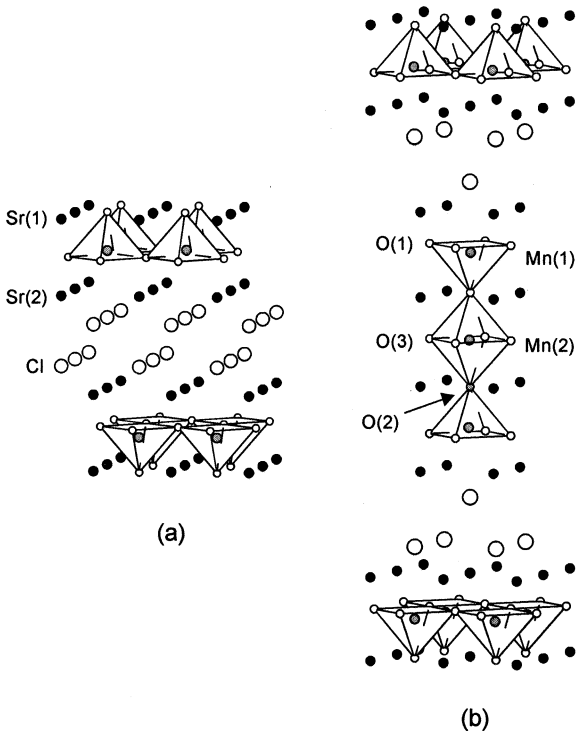

Figure 7. Crystal structures of Sr_2MnO_3Cl (a) and $Sr_4Mn_3O_8Cl_2$ (b). MnO_5 square-based pyramids and MnO_6 octahedra are shown.

of the single-layer material, through variation of sintering temperature and duration, failed to avoid completely the formation of a level of the three-layer phase. This probably reflects extremely small differences in the thermodynamic stability of these phases. Similar problems have been experienced in obtaining phase-pure Sr_2CoO_3Cl and $Sr_3Co_2O_5Cl_2$ samples.[8]

The structures of Sr_2MnO_3Cl and $Sr_4Mn_3O_{8-y}Cl_2$ are shown in Figure 7. Both compounds contain distorted $Mn(1)O_5$ square pyramids whose basal planes are separated by double SrCl layers. For Sr_2MnO_3Cl the larger chloride ion replaces one of the terminal apical oxygen positions of the perovskite block of the K_2NiF_4 phase Sr_2MnO_4. Ordering of the chloride ion along *z*, rather than random replacement of oxide, leads to a reduction of the cell symmetry from the *I*4/*mmm* of ideal K_2NiF_4 phases to *P*4/*nmm*. In $Sr_4Mn_3O_{8-y}Cl_2$ both terminal positions of the triple perovskite block are occupied by chloride, leaving the central Mn(2) to bond solely to oxygen. The Mn(1) coordination of both compounds may also be viewed as axially elongated MnO_5Cl octahedra, with the nonuniform coordination reflecting the presence of the large chloride ion rather than Jahn−Teller distortion.

The structural parameters for the single-layer material (Table 1) show no significant differences at room temperature from those previously presented in the communication.[10] Analysis of the neutron data has allowed the refinement of a strongly anisotropic ADP for the chloride ion, indicative of weaker potential minima in this layer and larger phonon modes. The neutron data also confirm the anion stoichiometry as O_3Cl, consistent with a manganese(III) oxidation state.

(16) Kriegel, R.; Feltz, A.; Walz, L.; Simon, A.; Mattausch, H. *Z. Anorg. Allg. Chem.* **1992**, *617*, 99.

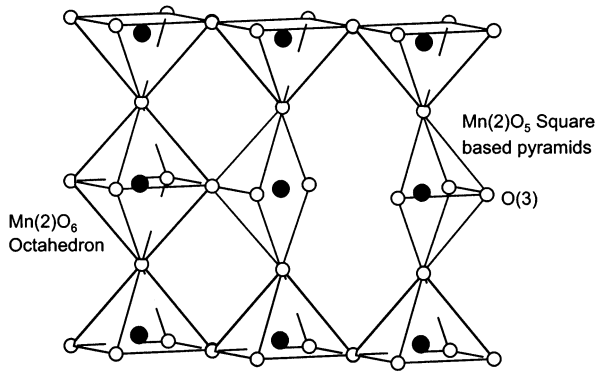

Figure 8. Effect of the basal oxygen O(3) vacancies on the local Mn(2)−Oxygen coordination.

On cooling, the basal Mn−O bond length exhibits a small decrease, reflecting the 0.02 Å reduction of the *a*-parameter, while the apical Mn−O distance and in-plane O(1)−Mn-O(1) bond angles remains static within experimental uncertainty. The contraction along the *c* direction is thus the result of a significant reduction in the SrCl layer separation overcoming the unexpected increase seen in the weak Mn−Cl interaction.

In contrast, analysis of the neutron data for the three-layer material has provided significant new information regarding the oxygen ion distribution within the phase. The results summarized in Table 2 reveal both site disorder and a level of oxygen deficiency associated with the basal oxygen of the nominal $Mn(2)O_6$ octahedra. Equivalent partial occupancy and site displacement of this basal oxygen has been observed for the analogous three-layer cobalt oxychloride.[8] The stoichiometry of the phase (based on the room-temperature occupancies) is $Sr_4Mn_3O_{7.56}Cl_2$, indicating the manganese valence is predominantly +3. Structurally, the consequence of the O(3) deficiency is reduction of the Mn(2) coordination from 6-fold to a mixture of 6- and 5-fold arrangements; that is, the site geometry will often be a square-based pyramid as shown in Figure 8. The small displacement refined for the in-plane oxygen along *x* may represent local relaxation of the square-pyramidal geometry toward trigonal bipyramidal or strain-induced rotations of oxygen complete $Mn(2)O_6$ units. The $Mn(1)O_5Cl$ octahedral unit present in $Sr_4Mn_3O_{8-y}Cl_2$ is similar to that found in the Sr_2MnO_3Cl but with slightly longer Mn−O(1) planar bonds and slightly shorter apical interactions (Table 3). The larger *a*-parameter found for the three-layer material allows a reduction in the buckling of the O(1)−Mn(1)−O(1) basal plane from 163° in Sr_2MnO_3Cl to 165°. The low-temperature results show the expected contraction in cell parameters and the majority of interatomic distances. The temperature dependence of the $Mn(1)O_5Cl$ is somewhat unusual as the apical Mn(1)−O(2) bond exhibits a small increase on cooling that is negated by an equivalent decrease in the apical Mn(1)−Cl interaction. Once more, there is evidence of anisotropy for the chloride ion motion with the refined thermal components, $U_{11} = U_{22} = 0.0026(4)$ Å^2 and $U_{33} = 0.0197(9)$ Å^2 at 2 K, indicating, in this material, strong vertical displacements of the atom.

The magnetic susceptibilities of Sr_2MnO_3Cl and $Sr_4Mn_3O_{8-y}Cl_2$ (Figures 3 and 4) provide strong evidence of antiferromagnetic correlations within the phases. Both materials show distinct maxima in χ at $T \approx 90$ K,

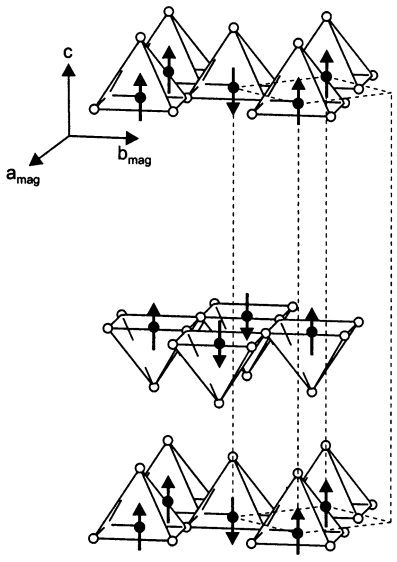

Figure 9. Magnetic cell of Sr_2MnO_3Cl showing the antiferromagnetically coupled Mn spins aligned along *z*. The nuclear cell is shown by the dotted lines.

characteristic of transitions to AF order, and the large negative Weiss constants (θ) determined from the high T region ($220 < T < 290$ K) indicate the presence of significant AF exchange coupling (Table 4). The calculated μ_{eff} values are both consistent with the presence of high-spin Mn(III). The slightly high value obtained for Sr_2MnO_3Cl may be linked to the presence of the small amount of the three-layer phase within the sample that was not corrected for when the effective moment was determined. The closeness of the ordering temperatures (T_{AF}) and θ values suggest the strength of the AF interactions within the phases is similar and is consistent with superexchange interactions propagating through their similar in-plane Mn(1)−O(1) bonds. A number of differences in the behavior of the susceptibility are apparent, with $Sr_4Mn_3O_{8-y}Cl_2$ displaying a sharper transition and a small degree of divergence between the ZFC and FC measurements below T_{AF}. The former possibly reflects the higher dimensionality of the manganese sublattice present in the material while the latter implies a degree of spin-glass behavior accompanies the AF transition. The paramagnetic tail in χ at $T < 50$ K seen for both samples is similar to that observed for the isovalent $Ba_xSr_{1-x}LaMnO_4$ ($0 \leq x \leq 0.29$) solid solution[17] and could be linked to a fraction of isolated spins.

The low-temperature neutron diffraction patterns (Figures 5 and 6) confirm the presence of long-range AF order; however, the similarities apparent from the susceptibility data are not reflected in the magnetic scattering of the phases. We first consider the single-layer phase for which the analysis has been straightforward. On the basis of the magnetic Bragg peaks detected at 2 K, it has been possible to determine a magnetic structure for the phase. The compound adopts a magnetic superlattice commonly exhibited by K_2NiF_4-type materials with nearest neighbor Mn spins AF coupled in the tetragonal plane and along *z* (Figure 9). The refined moment $\mu_z = 3.74(5)\ \mu_B$ lies in the accepted range for a $3d^4$ ion and indicates that the majority of the moments are long-range ordered at this temperature. Some reduction in the moment measured by neutron diffraction from the theoretical 4.9 μ_B is expected due to covalency effects and possible spin disorder. In comparison, a moment of 3.3 μ_B was obtained for the K_2NiF_4 phase $LaSrMnO_4$ at 10 K.[17]

The magnetic scattering exhibited by $Sr_4Mn_3O_{8-y}Cl_2$ in comparison is limited to the intensity at 5.2 and 5.4 Å (the peak at 5.1 Å originates from the impurity MnO). The magnetic reflections are weak relative to the neighboring nuclear reflections (in contrast, the magnetic Bragg peaks observed for Sr_2MnO_3Cl are among the most intense seen in the A-bank) and this suggests a degree of disorder is present in the system. Certainly, the appreciable oxygen deficiency of $Sr_4Mn_3O_{7.56}Cl_2$ provides support for this interpretation. The refined partial occupancy of the basal O(3) site results is an approximate 1 in 4 chance of the site being a vacancy and consequently the Mn(2)−O(3)−Mn(2) superexchange pathways are, as shown by Figure 8, severely disrupted. The structural disorder in this plane is likely to further inhibit the truly long-range 3-D correlations important to the observation of magnetic reflections. Another factor that may play a role in diminishing the coherent magnetic scattering from the phase becomes apparent if the possible interlayer coupling pathways are considered (Figure 7b). For $Sr_4Mn_3O_{8-y}Cl_2$ there are two equivalent ways of antiferromagnetically coupling the Mn(1) spins in one block to those in a neighboring block and in the absence of local distortions these interactions are frustrated. From the current evidence the magnetism of $Sr_4Mn_3O_{8-y}Cl_2$ is intermediate between a long-range ordered system and a spin-glass with strong AF interactions present in its domains.

The differing magnetic scattering exhibited by the phases allows a more accurate appraisal of the significance of the transition temperatures determined from the susceptibility data. For the single-layer material the determination of a three-dimensional magnetic structure with a significant ordered moment at 2 K strongly suggests that T_{AF} is associated with a transition to long-range AF order, that is, $T_{AF} = T_N$, as found for the related $Ba_xSr_{1-x}LaMnO_4$ series.[17] In comparison, the transition temperature determined for the three-layer phase appears to signify the appearance of regions of antiferromagnetically ordered spins that are large enough to give some coherent scattering at 2 K. However, a level of disorder and/or frustration within the compound prevents it from being described as a truly long-range ordered system.

In light of the results presented in this study we are now in a better position to assess the oxychlorides in relation to their suitability as potential CMR phases. Most significantly, the neutron diffraction analyses have confirmed that the oxidation state of Mn in the phases is almost exclusively +3, in contrast to known RP CMR manganates which possess a mixed valence state typically in the range ca. +3.2−3.5.[11,12] The absence of a mixed Mn valence state is likely to preclude magnetoresistance as the introduction of a significant level of Mn(IV) appears to be critical for the observation of

(17) Bieringer, M.; Greedan, J. E. *J. Mater. Chem*. **2002**, *12*, 279.

magnetotransport effects.[18] In this regard the synthesis of oxygen stoichiometric $Sr_4Mn_3O_8Cl_2$ would be of considerable interest, yielding a material with a manganese valence state of +3.33 and probably, based on coordination environments, a level of Mn(IV) localized on the Mn(2) site. The subsequent removal of the in-plane O(3) vacancies would also create extended Mn(2)−O(3)−Mn(2) pathways, enhancing the possibility of CMR. One other feature, evident from the crystal structures of the oxychlorides, that will play a role in determining the electronic properties they display are the highly buckled $Mn(1)O_2$ square planes. The basal Mn(1)−O(1)−Mn(1) bond angles show a significant (≈15°) distortion that will reduce orbital overlap and may limit electron delocalization.

In summary, the crystal structures of the manganese oxide chlorides Sr_2MnO_3Cl and $Sr_4Mn_3O_{8-y}Cl_2$ have been determined from Rietveld analysis of neutron powder diffraction data collected at room temperature and 2 K. The level of oxygen deficiency within $Sr_4Mn_3O_{8-y}Cl_2$ has been determined, that is, $y = 0.44(2)$, and found to be localized in the basal plane of its central $MnO_{6-\delta}$ octahedra. Susceptibility data indicate the onset of antiferromagnetic correlations in both phases at $T \approx 90$ K and magnetic order is confirmed by additional intensity in the low-temperature neutron diffraction patterns. Sr_2MnO_3Cl adopts a magnetic structure similar to that of the related antiferromagnet $LaSrMnO_4$ while the magnetic scattering of $Sr_4Mn_3O_{8-y}Cl_2$ is indicative of a level of spin disorder and possible magnetic frustration. Of the two systems, $Sr_4Mn_3O_{8-y}Cl_2$ is the more promising candidate for developing magnetotransport effects and studies aimed at the synthesis of stoichiometric $Sr_4Mn_3O_8Cl_2$ are currently in progress.

Acknowledgment. The authors thank the EPSRC for Grant GR/M21836 in aid of this work and for the provision of neutron beam time at the ISIS facility. In addition, we thank Prof. P. A. G. De Groot, Department of Physics and Astronomy, University of Southampton, for access to the SQUID magnetometer and Dr. D. J. Price, Department of Chemistry, University of Southampton, for helpful discussions relating to magnetism.

CM020280C

(18) Battle, P. D.; Green, M. A.; Laskey, N. S.; Kasmir, N.; Millburn, J. E.; Spring, L. E.; Sullivan, S. P.; Rosseinsky, M. J.; Vente, J. F. *J. Mater. Chem*. **1997**, 7, 977.